ACS OMEGA

http://pubs.acs.org/journal/acsodf

Article

Fabrication of Hierarchical Lignin-Based Carbon through Direct High-Temperature Pyrolysis and Its Electrochemical Application

Rui Lou,* Jie Tian, Yanan Zhang, and Wei Chen*

Cite This: *ACS Omega* 2021, 6, 34129−34136

Read Online

ACCESS | Metrics & More | Article Recommendations | Supporting Information

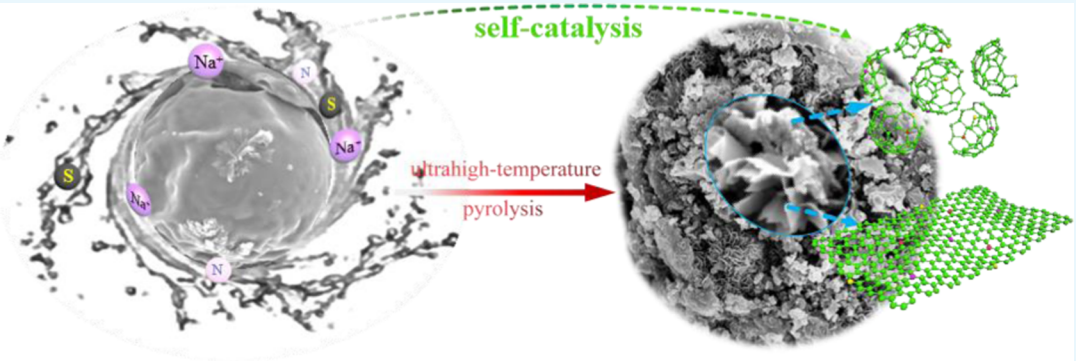

ABSTRACT: Green synthesis of lignin-based carbon materials can accelerate the development of energy storage and conversion in supercapacitors. In this work, hierarchical graphenelike carbon was prepared by alkali lignin (AL) pyrolysis at a high temperature of 1700 °C. Accompanied by metal salt catalysis and a nitrogen hybridization reaction, a unique nanostructure of graphitized ALC was obtained with both a well-ordered 2D sheet lamellar structure and a uniform bowl-like porous structure. ALC exhibited a graphenelike lattice structure, a BET specific surface area of 1190 $m^2 \cdot g^{-1}$, and excellent electrochemical performance (104 $F \cdot g^{-1}$/0.5 $A \cdot g^{-1}$). The study offers a prospective way to the high-value application of industrial lignin in supercapacitor electrode materials.

INTRODUCTION

As a sustainable biopolymer and a nonvalorized byproduct of the paper and pulp industry, alkali lignin (AL) comes from black liquor in the kraft pulp process where wood chips or straw stalks are heated for 1−3 h in sodium hydroxide and sodium sulfide after which the cellulose is removed.[1] However, only 2% of its production is being commercialized in low-value products.[2] Thus, developing bioproducts from lignin feedstocks is an essential part of an integrated biorefinery, which not only diversifies the portfolio of products and markets but also keeps processing cost-effective and encourages the holistic utilization of wastes as part of the development of circular economies.[3]

Lignin is the most abundant aromatic biopolymer with its structure rendering it ideal for carbon production, depending on high carbon content (up to 60%).[2,4] Thus, lignin can be transformed into functional carbon or composite materials, which have promising applications as biofuels, chemicals, and biomaterials. At present, the hierarchical porous carbon derived from lignin has emerged increasingly in applications in supercapacitors and lithium batteries as electrode material because of its high surface area, excellent superior electrical conductivity, and high chemical stability.[5−7] For example, Zhang et al. prepared carbon electrodes from AL direct pyrolysis at 700 °C and activated AL with KOH. With the addition of KOH, the specific surface area of carbon materials increased from 77.1 to 907.0 $m^2 \cdot g^{-1}$, and the resulting specific capacitance was improved from 25.7 to 168.2 $F \cdot g^{-1}$.[5] Li et al. fabricated tunable hierarchical porous carbons from kraft lignin pyrolysis at 900 °C with a P123 template and silica nanoparticles, which had the specific surface area of porous carbon of 645 $m^2 \cdot g^{-1}$, and the prepared working electrode had an excellent volume specific capacitance of 104.5 $F \cdot cm^{-3}$.[6] Besides, Li et al. prepared hierarchical porous carbon materials derived from woody lignin (pine/poplar) pyrolysis with KOH activator under 700 °C, revealing that lignin with a high S/G monomer ratio contributed to generating carbon, which had a higher specific surface area of 621.3 $m^2 \cdot g^{-1}$ and a good specific capacitance of 86.7 $F \cdot g^{-1}$.[7] In short, to obtain a higher specific surface area and an excellent specific capacitance property, the above preparation methods of lignin-based carbon used some templates and surfactants in the process of porous carbon

Received: October 13, 2021
Accepted: November 25, 2021
Published: December 5, 2021

ACS Publications

© 2021 The Authors. Published by American Chemical Society

https://doi.org/10.1021/acsomega.1c05730
ACS Omega 2021, 6, 34129−34136

preparation, but this likely caused some potential environmental pollution and an increase of the stock cost.

Moreover, researchers found that some metals or metal salts as catalytic intermediates could facilitate the formation of graphene carbons in the process of lignin pyrolysis/carbonization, and graphene carbons exhibit outstanding advantages in electrochemical properties.[8−12] Zhao et al. used lignin from straw biorefining residues as a carbon precursor to prepare graphene carbon with ferric nitrate catalyst at a pyrolysis temperature of 900 °C, and the obtained carbon as a working electrode had a good specific capacitance of 183.1 $F{\cdot}g^{-1}$ under a current density of 1 $A{\cdot}g^{-1}$.[8] Wang et al. reported that calcium sulfide nanoparticles as a catalyst could trigger the graphene layer in situ formation in calcium lignosulfonate pyrolysis and carbonization in a temperature range of 1100−1500 °C.[9] Thus, carbon with graphene or a nanographite structure was produced from lignin feedstocks at a high pyrolysis temperature coupled with metal catalysts.[10] For instance, Jeong et al. elaborated the significant catalytic effect of alkali and alkaline earth metals in lignin pyrolysis by the density functional theory method and revealed that alkali and alkaline earth metals, including magnesium, potassium, sodium, and calcium, catalyzed the bond-breaking mechanism, and yet their influences on generating char or carbon formation were not elaborated.[11]

In general, sodium salts can be considered as a part of AL because sodions (Na^+) connect with phenolic hydroxyl groups and carboxyl acid groups of lignin by chemical bonds, forming phenolic sodium and carboxylate sodium groups.[12] Thus, AL has a variable phenylpropane structure and contains small amounts of metal salts for the varied pulping process and lignin separation conditions from black liquor. Hence, in this work, based on the catalyzed effect of metal salts, AL containing certain sodium metals was used as the carbon precursor, through direct pyrolysis at a higher temperature of 1700 °C, to prepare the hierarchical carbon material. The microstructure, chemical compositions, and electrochemical performances of the resultant carbon were elaborated in detail.

RESULTS AND DISCUSSION

Elemental Composition and Chemical Structure of ALC. After AL was pyrolyzed and carbonized under a N_2 atmosphere at a high temperature of 1700 °C, almost all groups' absorption peaks disappeared in the AL-based carbon (ALC) spectrum (Figure 1). During AL pyrolysis and the carbonization process, the homolysis and condensation reactions occurred, accompanied by a repolymerization reaction of the intermediates to reform graphitic carbon frameworks.[13] The gasified carbonic oxide, alkyl hydrocarbons, and aldehyde/acid compounds escaping from AL pyrolysis at 800−1000 °C become carbon sources to produce graphenelike carbon by vaporization and carbonization in a high-temperature range of 1200−1700 °C. It is clearly observed that the wide band (3530 cm^{-1}) for the hydroxyl groups' (−OH) in-plane bending and distinct bands (2941, 1600−1400, 1121, and 840 cm^{-1}) representing the intrinsic aromatic properties of ALC completely disappeared. Consequently, the C−C bond and C−O bond linkages of substituents were cleaved from aromatic rings at high temperatures.[14] The ensuing stable C−C bond was rearranged to a benzene ring structure (1600 cm^{-1}), and the region of 800 cm^{-1} resulted from the aggregated edge-oxidized structure by epoxy ether configuration and an increase of graphene layers.[15]

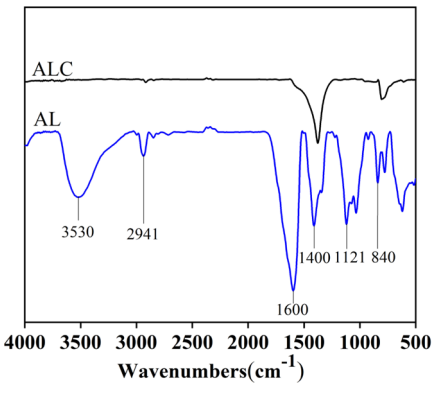

Figure 1. FTIR spectra of ALC and AL.

ALC was obtained with a yield of 30.92% as AL was pyrolyzed and carbonized under a N_2 atmosphere at 1700 °C. It can be seen from Table 1 that oxygen of 33.24 wt % and sodium of 14.32 wt % were greatly lost during the AL pyrolysis and carbonization process. Na was mainly in the form of Na_2CO_3 and NaCl in AL. In the process of pyrolysis and carbonization, inherent Na salts played a significant role as the template and catalyzed the formation of graphene structures in ALC. As the pyrolysis temperature was high up to 1700 °C, Na_2CO_3 and NaCl salts decomposed to sodium metal to evaporate out ALC.[16] Thus, sodium salts in AL favored the formation of a porous carbon structure. It is worth noting that the nitrogen content was significantly increased in ALC, indicating that N-doping occurred in carbon atoms. Perhaps the reason for this was that nitrogen atoms exposed at a high temperature of 1700 °C became active in the hybridization reaction. Nitrogen introduced into the activated carbon could induce additional pseudocapacitance via a reversible redox reaction and improve the wettability between the electrodes and the electrolytes, thereby improving the electrochemical performance of porous carbon.[17]

Morphology and Nanostructure of ALC. The morphology of ALC was obtained using SEM and is displayed in Figure 2b. The unique nanostructure of ALC was obtained through direct pyrolysis at 1700 °C, which consisted of both 2D sheet graphene with a roselike feature (Figure 2a) and uniform bowl-like carbon with an interconnected porous structure (Figure 2c). One interesting finding is that the oriented 2D sheet carbon with a bloomy roselike structure of these graphitized lamellas might be ascribed to the catalytic effect of alkali metals (K^+, Na^+), which remained coherent in AL as catalyst intermediates combining with some sulfur and nitrogen inducing atomic nanohybridization.[18,19] This result likely was similar to iron powder catalyzed to generate graphene carbon in kraft lignin pyrolysis reported by Liu et al., with 2D sheet-layer nanocarbon formed in the process of lignin pyrolysis with metallic catalysis.[20] In addition, porous carbon materials were prepared from lignin that was passed through an activation process by metal salts (such as Na^+, K^+, Zn^+, etc.) in an inert atmosphere. Thus, a large amount of oxygen-containing functional groups in lignin and the metal salt template self-assembled into precursors through a hydrogen bond interaction and finally formed porous carbon with a bowl-like structure derived from AL by pyrolysis and carbonization at a high temperature of 1700 °C.[21]

https://doi.org/10.1021/acsomega.1c05730
ACS Omega 2021, 6, 34129−34136

Table 1. Elemental Composition of ALC and AL Using SEM-EDS

elementals		C	N	O	S	Na	K	Si	Cl	Ca
AL	wt %	45.74	1.83	33.24	1.53	14.32	1.73	0.55	0.84	0.03
	at. %	56.18	1.92	30.65	0.70	9.19	0.65	0.29	0.35	0.01
ALC	wt %	81.57	11.64	2.93	0.95	0.51		1.61		0.12
	at. %	85.51	10.46	2.31	0.37	0.28		0.72		0.04

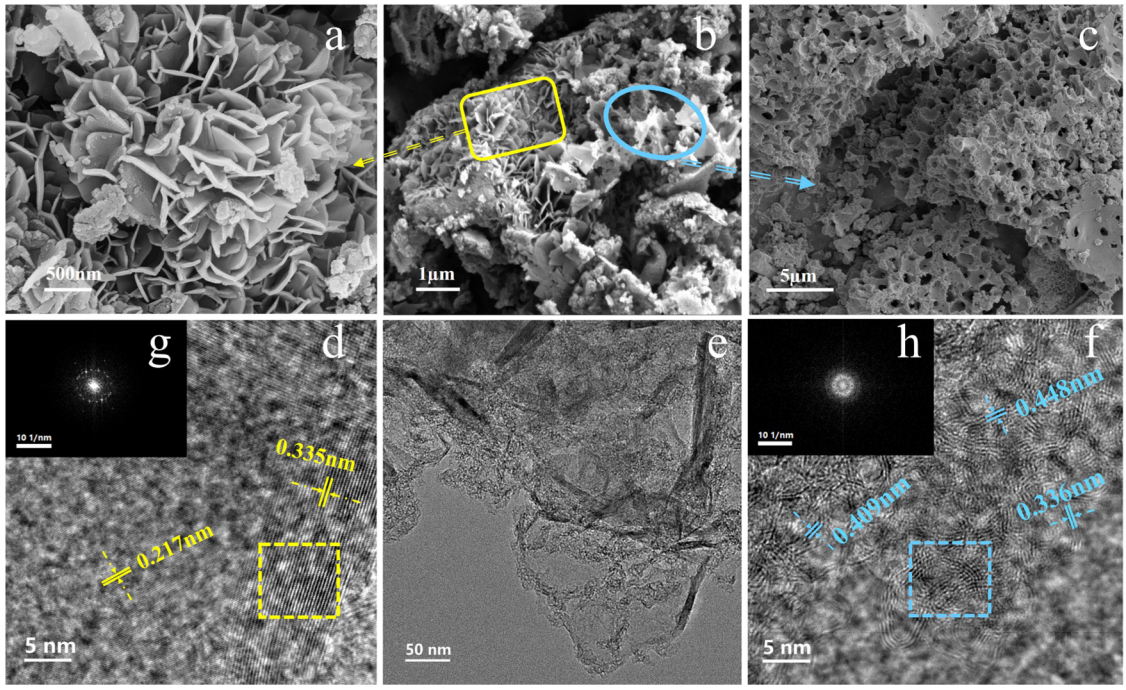

Figure 2. Microstructure features of ALC (SEM images (a–c) and TEM (e) and HRTEM (d, f) images with FFT diffraction patterns (g, h)).

For a better understanding of the microstructure features of ALC, TEM and HRTEM images were used to observe the microappearance and lattice fringes. Figure 2b shows that the hybrid nanostructure of ALC consisted of a 2D stereo laminated structure and a porous structure. 2D sheet carbon covered some well-ordered lamellar structures in the form of graphene. These stacked graphene sheets and few monolayers had a long-range ordered feature (Figure 2d), and the corresponding lattice *d*-spacing was demonstrated to be approximately 0.335 and 0.217 nm in the interplanar spacing of (002) and (101−103) planes, respectively. Amorphous carbon with small graphitic nanocrystal domains showed short-range ordered and some disordered features with *d*-spacings of 0.336−0.448 nm (Figure 2f).[22,23] Furthermore, the obtained FFT diffraction patterns of carbon showed distinctively the diffraction spots of graphene structure (Figure 2g) and the bright rings of amorphous graphitic carbon (Figure 2h).[24] The obtained carbon nanostructure was consistent with those previously reported.[22,25] Therefore, this finding confirms that the alkali metals (K^+, Na^+) remaining coherent in AL had a significant catalytic effect on the formation of graphene layers. Moreover, many macropore channels from blooming roselike graphene layers can be effective to block graphenelike carbon restacking and introduce more active sites, which serve as electrolyte ion-buffering reservoirs in the electrochemical process. The hierarchical bowl-like carbons with a mesoporous structure can also provide the shortest ion transmission path.[26,27] Thus, the unique nanostructures of ALC are favorable for better electrochemical performance.

XRD patterns (Figure 3a) revealed that ALC contained peaks in crystallographic planes of (002), (010), (011), (004), and (013), corresponding to the respective 2θ position of 26.5, 41.5, 44.1, 54.7, and 60.1°. The sharp peak at 26.5° had the highest intensity attributed to the interplanar spacing of the (002) plane for ordered graphene in ALC, corresponding to the *d*-spacing of 0.335 nm between the graphenelike 2D sheets. These broad peaks of 41−45° were ascribed to (101−103) lattice planes with the *d*-spacing of 0.208−0.217 nm, attributed to the initial evolution of amorphous carbon into ordered graphitic structures, which were typical of layered graphenelike sheets with the metallic feature.[6,28] Other peaks (2θ = 33.4, 35.6, 38.1, and 60.1°) in the scattering pattern can be attributed to the presence of the detected sodium and silicon carbide.

Graphitization degree and lattice spacing are of more prime importance for lignin-based anodes in addition to the specific surface area.[21] I_D/I_G is an important index to estimate the disorder degree of carbon materials, that is, the intensity ratio of D-band (amorphous carbon) and G-band (graphenelike carbon).[29,30] The I_D/I_G of ALC was 1.16. The D-band at 1350 cm^{-1} corresponded to sp^2 and sp^3 hybrid carbon, depending on the irregular arrangement degree and lattice defects of graphene. The D-band intensity became stronger with an increase of lattice defects and the disorder degree. Furthermore, the peak existence of both the 2D-band at 2671 cm^{-1} and the D+D′-band at 2931 cm^{-1} (Figure 3b) surely confirmed that the multilayer stacked graphene carbon was formed in AL pyrolysis at 1700 °C and had the well-

https://doi.org/10.1021/acsomega.1c05730
ACS Omega 2021, 6, 34129−34136

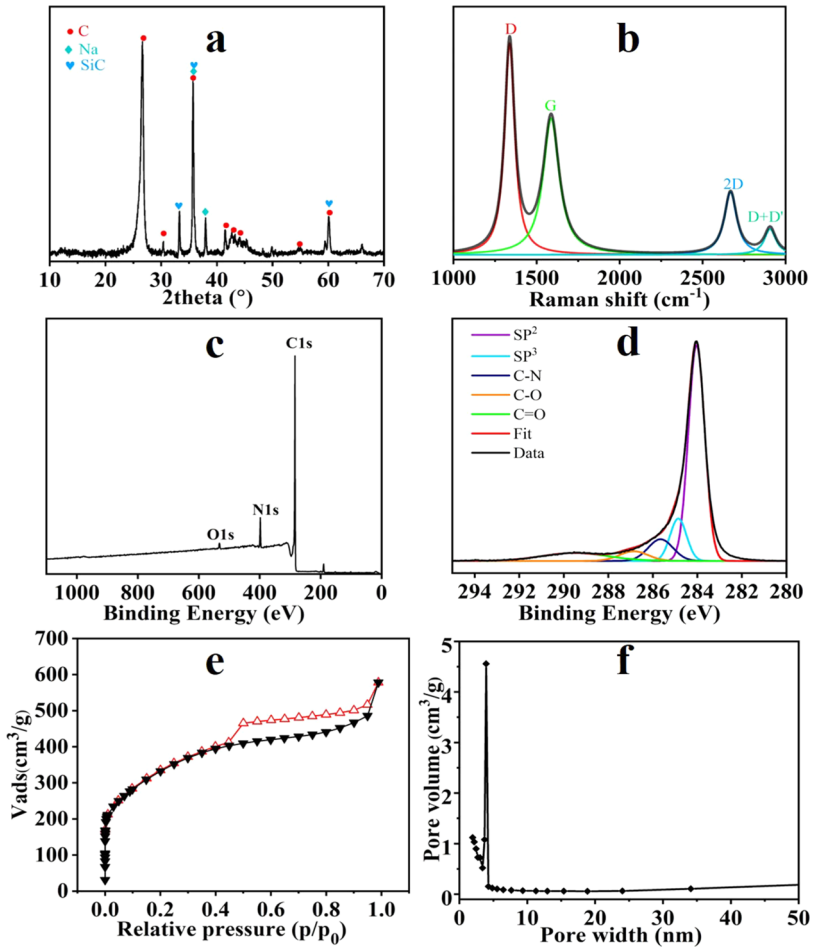

Figure 3. Detected spectral signatures of ALC ((a) XRD pattern, (b) Raman spectrum with fitted Lorentz peaks, (c) the overall profile of the XPS spectrum, (d) high-resolution XPS spectra of C 1s, (e) N_2 adsorption−desorption isotherm, and (f) porosity size distribution).

ordered long-range and short-range graphene structure. The alkali metals (Na^+, K^+) forming phenolic sodium and carboxylate sodium groups as organically bound in AL played a significant role in catalyzing the crystal carbon growth during the high-temperature pyrolysis process.[31] The sodion and potassium could increase the C−O ether bond distance and decrease the C−C bond distance, contributing to the boundary defects and lattice splitting in the graphenelike carbon nanostructure in the D-band.[31] Slight amounts of oxygen (C−O) contained in ALC benefit the adsorption of electrolyte ions and redox reactions in the carbon-based electrode.[5]

The compositions and chemical states of ALC were further analyzed using XPS (Figure 3c). ALC was composed of 91.67% carbon, 1.30% oxygen, and 7.02% nitrogen, consistent with the results from EDS mapping. A small amount of oxygen and a certain amount of nitrogen remained in ALC derived from the carbon precursor of AL, suggesting that most of the oxygen had evaporated during the AL pyrolysis process at a temperature up to 1700 °C, while nitrogen hybridized the formation of the carbon to trigger the graphene nanostructure growth.[32] Besides, the C/O atomic ratio in ALC was as high as 70, demonstrating that ALC formed a higher graphitization structure and complete decomposition of oxygen-containing functional groups had occurred during lignin carbonization at 1700 °C. The high-resolution scan of the C 1s region can be deconvoluted into five predominant peaks at 284.0, 284.8, 285.6, 286.8, and 289.5 eV, corresponding to the respective C-sp^2 (69.4%), C-sp^3 (12.5%), C−N (6.6%), C−O (5.0%), and C═O (6.5%).[33,34] Among these peaks, primary sp^2 and sp^3 graphitic carbons were ascribed to the conjugated C═C bond and C−C bond, respectively, the C−N peak corresponded to the bonding of doped nitrogen atoms to sp^2 carbon,[10] and C−O ether bond and C═O bond were attributed to oxygen singly/doubly bonded to aromatic carbon (phenolic and aliphatic groups) that was distributed in the boundary of the lattice structure, consistent with the findings from FTIR results that the marked epoxy ether bonds existed in the boundary of graphene carbon.

The specific surface area and porosity size distribution of ALC were investigated using nitrogen adsorption−desorption isothermal analysis (Figure 3e). ALC showed a I/IV-type isotherm with a H2 hysteresis loops in p/p_0 of 0.5−1.0. The specific surface area of ALC was 1190 $m^2 \cdot g^{-1}$ as calculated using the Brunauer−Emmett−Teller (BET) method. ALC showed a total pore volume of 0.80 $cm^3 \cdot g^{-1}$ and a mesopore distribution at 3.85 nm, along with a high mesopore rate of ∼93% by the BJH method. The results agreed well with the bowl-like morphology of ALC with a large number of mesopores.[30] The hierarchical and interconnected pore structure of ALC, i.e., high graphitization and high mesopore volume (0.74 $cm^3 \cdot g^{-1}$), could better enhance capacitive deionization performance and form a good ion transfer pathway to shorten the ion diffusion distance, thus accelerating ion transport.[35]

https://doi.org/10.1021/acsomega.1c05730
ACS Omega 2021, 6, 34129−34136

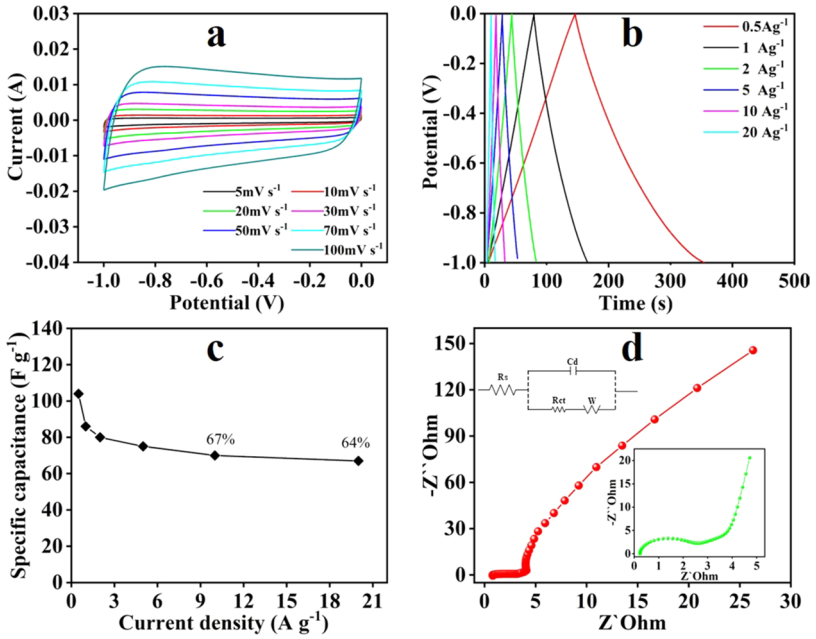

Figure 4. Electrochemical properties of the ALC electrode ((a) CV curves at various scan rates, (b) GCD curves at the current density of 0.5−20 $A{\cdot}g^{-1}$, (c) specific capacitance vs current densities, and (d) Nyquist plots over the frequency range of 0.01−50 kHz).

Electrochemical Performance. To reveal the electrochemical properties of ALC, the electrochemical performances of cyclic voltammetry (CV), galvanostatic charging/discharging (GCD), and electrochemical impedance spectroscopy (EIS) were measured in a three-electrode system. Figure 4a displays these CV curves in a potential window ranging from −1 to 0 V at a scan rate of 5−100 $mV{\cdot}s^{-1}$. Obviously, all CV curves could still maintain a rectangular-like shape even at a high scan rate of 100 $mV{\cdot}s^{-1}$, indicating that ALC had excellent rate capability and charge response speed.[36] The symmetrical isosceles triangle of all GCD curves presented in Figure 4b indicated that the ALC electrode displayed excellent electrochemical reversibility.[37] When the current density was 0.5 $A{\cdot}g^{-1}$, the specific capacitance of ALC was maximum at 104 $F{\cdot}g^{-1}$, whereas when the current density was 5 $A{\cdot}g^{-1}$, the specific capacitance decreased to 70 $F{\cdot}g^{-1}$.

It was obvious that the specific capacitance of ALC decreased with an increase in current density (Figure 4c), due to the active sites weakening as the current density increased because of the limited ion diffusion at the electrode/electrolyte interfaces resulting in the unavoidable drop in capacitance.[38] Even so, the working electrode of ALC showed high capacitance retention (i.e., 67% at 10 $A{\cdot}g^{-1}$ and 64% at 20 $A{\cdot}g^{-1}$) and excellent electrochemical performance at high current density. Compared with other results (Table 2), the ALC electrode in this work had a higher specific capacitance.

Electrode conductivity and ion diffusion are greatly important for the capacitance and capacitive deionization performances of electrode materials.[35] Figure 4d shows that the EIS curve of Nyquist plots over the frequency range indicated a semicircle in the high-frequency range and a straight line in the low-frequency range. The high slope of the curve at low frequency meant small ion diffusion resistance, high electrode conductivity, and electron transfer rates. Besides, the equivalent electrical circuit (the inserted fitted line) comprises a series of resistance (R_s), charge transfer resistance (R_{ct}), Warburg impedance (W), and double-layer capacitance (C_d).[44] In the high-frequency region, the lower R_{ct} = 0.5 Ω and R_s = 0.7 Ω suggested that the ALC electrode had a fast charge transfer ability and high conductivity. The above results indicated that the ALC electrode had high electrode conductivity, excellent electron transfer rates, and small ion diffusion resistance because of faster ion transport in the ALC electrode with a higher mesopore rate and lower resistance,[45] thus, ALC application in the supercapacitor field is greatly promising.

Table 2. Electrochemical Performances of Lignin-Based Carbons

feedstock	activation	electrolyte	capacitance ($F{\cdot}g^{-1}$/$A{\cdot}g^{-1}$)	references
alkali lignin		6 M KOH	104/0.5	this work
alkali lignin		6 M KOH	64/0.4	39
kraft lignin		1 M H_2SO_4	91/0.5	40
ethanol-extracted lignin		1 M H_2SO_4	35/0.5	40
alkali lignin		1 M H_2SO_4	53/0.5	40
sodium-lignosulfonate		6 M KOH	17/1.0	41
woody lignin	KOH	1 M H_2SO_4	48−87/0.5	42
kraft lignin	KOH	1 M NaCl	73/0.5	43

CONCLUSIONS

Hierarchical graphenelike porous ALC was fabricated using high-temperature pyrolysis combined with self-catalysis of metal salts and nitrogen hybridization reactions. The unique nanostructure of ALC consisted of the well-organized graphene 2D sheets with a roselike feature and the interconnected bowl-like carbon with uniform mesoporous structure, exhibiting a high specific surface area and excellent specific capacitance and electrochemical reversibility. Therefore, AL as a carbon precursor is available to prepare electrode material, and the simple and eco-friendly conversion method provides a prospective way to produce lignin-based carbon electrode materials.

https://doi.org/10.1021/acsomega.1c05730
ACS Omega 2021, 6, 34129−34136

EXPERIMENTAL SECTION

Preparation of Materials. Alkali lignin (AL) was collected from wheat straw pulping of the Quanlin Paper Industry Group of Shandong province in China. AL pyrolysis was carried out in a vacuum sintering furnace (ZT-40-21Y, HIGH MULTI 5000, Japan) at a higher temperature of 1700 °C in a nitrogen atmosphere. Prior to nitrogen blowing into the furnace, the air in the furnace was pumped out. The AL pyrolysis test began when the furnace pressure was stabilized at atmospheric pressure (~100 kPa). The experimental program was set as follows: pyrolysis temperature from atmospheric temperature with a heating rate of 10 °C·min^{-1} heated up to 800 °C, kept for 30 min, continuously increased to 1400 °C, then at a heating rate of 5 °C·min^{-1} heated up to 1700 °C, and kept for 60 min. Afterward, the temperature decreased to 600 °C with 10 °C·min^{-1}, and then the furnace was cooled to room temperature.

Characterization. Surface morphology and the compositions were analyzed using field emission scanning electron microscopy (SEM; FEI Verios 460) combined with energy-dispersive spectroscopy (EDS). Transmission electron microscopy (TEM; FEI Tecnai G2 F20 S-TWIN) coupled with high-resolution transmission electron microscopy (HRTEM) was used to observe the microstructure of ALC, and the diffraction mottling was determined by a digital micrograph method based on HRTEM image transformation with fast Fourier transform (FFT). The crystal structure was determined using X-ray diffraction (XRD; Bruker D8 Advance) with Cu Kα radiation at 40 kV and 40 mA (1.5406 Å). Raman spectra were acquired on a Raman microspectrometer (DXRxi) using argon ion laser (523 nm). X-ray photoelectron spectroscopy (XPS; Thermo Scientific) with Al Kα (1486.6 eV) radiation was performed to analyze binding energy with the fitting of Gaussian peaks. Fourier transform infrared (FTIR; Bruker Vertex 70) spectrograph was obtained to detect structural groups. The specific surface area and porosity were detected on an automated gas sorption analyzer (ASAP 2460 sn:506) with a flow of nitrogen at 200 °C for 7 h.

Electrochemical Measurements. For the three-electrode system, the working electrode was prepared by mixing ALC (40 mg), polytetrafluorethylene (PTFE) binder, and acetylene black in a mass ratio of 8:1:1. The resultant homogenized mixture was coated onto a nickel foam and dried at 120 °C for 12 h. Finally, a three-electrode electrochemical setup with KOH electrolyte (6 M), platinum coil as a counter electrode, and saturated Hg/HgO electrode as a reference electrode was evaluated for its electrochemical property. CV, GCD, and EIS of the ALC electrode were determined on a CHI 660E electrochemical workstation (Shanghai CH Instruments, China). CV curves were obtained within a potential window of −1 to 0 V at a scan rate of 5−100 mV·s^{-1}, along with GCD curves at the current density of 0.5−20 A·g^{-1} and electrochemical impedance spectra at an open-circuit voltage in the frequency range of 10^5−10^{-2} Hz. The specific capacitance was calculated using eq 1.

$$C = \frac{I_d \times \Delta t}{\Delta U \times m} \quad (1)$$

where C is the gravimetric specific capacitance, F·g^{-1}; I_d is the discharge current, A; Δt is the discharge time, s; ΔU is the discharge voltage range, V; and m is the mass of active ALC loaded on nickel foam, g.

ASSOCIATED CONTENT

Supporting Information

The Supporting Information is available free of charge at https://pubs.acs.org/doi/10.1021/acsomega.1c05730.

Particle size distribution of AL (Figure S1); SEM image of AL (Figure S2); and elemental compositions of AL (a) and ALC (b) using SEM-EDS (Figure S3) (PDF)

AUTHOR INFORMATION

Corresponding Authors

Rui Lou − *College of Mechanical and Electronic Engineering, Shaanxi University of Science and Technology, Xi'an 710021, P. R. China*; orcid.org/0000-0002-8494-9656; Email: lourui@sust.edu.cn

Wei Chen − *College of Mechanical and Electronic Engineering, Shaanxi University of Science and Technology, Xi'an 710021, P. R. China*; Email: chenweijd@sust.edu.cn

Authors

Jie Tian − *College of Mechanical and Electronic Engineering, Shaanxi University of Science and Technology, Xi'an 710021, P. R. China*

Yanan Zhang − *Shaanxi Key Laboratory of Chemical Additives for Industry, College of Chemistry & Chemical Engineering, Shaanxi University of Science and Technology, Xi'an 710021, P. R. China*

Complete contact information is available at: https://pubs.acs.org/10.1021/acsomega.1c05730

Notes

The authors declare no competing financial interest.

ACKNOWLEDGMENTS

This work was largely supported by the Key Research and Development Program of Shaanxi Province of China (No. 2021SF-502) and Open Project Fund of Guangxi Key Laboratory of Clean Pulp and Papermaking and Pollution Control of Guangxi University (No. 2021KF35).

REFERENCES

(1) Baliga, V.; Sharma, R.; Miser, D.; Mcgrath, T.; Hajaligol, M. Physical characterization of pyrolyzed tobacco and tobacco components. *J. Anal. Appl. Pyrolysis* **2003**, *66*, 191−215.

(2) Culebras, M.; Ren, G.; O'Connell, S.; Vilatela, J. J.; Collins, M. N. Lignin doped carbon nanotube yarns for improved thermoelectric efficiency. *Adv. Sustainable Syst.* **2020**, *4*, No. 2000147.

(3) Sajjadi, M.; Ahmadpoor, F.; Nasrollahzadeh, M.; Ghafuri, H. Lignin-derived (nano) materials for environmental pollution remediation: current challenges and future perspectives. *Int. J. Biol. Macromol.* **2021**, *178*, 394−423.

(4) Xi, Y.; Huang, S.; Yang, D.; Qiu, X.; Su, H.; Yi, C.; Li, Q. Hierarchical porous carbon derived from the gas-exfoliation activation of lignin for high-energy lithium-ion batteries. *Green Chem.* **2020**, *22*, 4321−4330.

(5) Zhang, W.; Lin, H.; Lin, Z.; Yin, J.; Lu, H.; Liu, D.; Zhao, M. 3D hierarchical porous carbon for supercapacitors prepared from lignin through a facile template-free method. *ChemSusChem* **2015**, *8*, 2114−2122.

(6) Li, H.; Zhao, Y.; Liu, S.; Li, P.; Yuan, D.; He, C. Hierarchical porous carbon monolith derived from lignin for high areal capacitance supercapacitors. *Microporous Mesoporous Mater.* **2020**, *297*, No. 109960.

(7) Li, W.; Zhang, Y.; Das, L.; Wang, Y.; Mi, L.; Wanninayake, N.; Pu, Y.; Kim, D. Y.; Cheng, Y. T.; Ragauskas, A. J.; Shi, J. Linking lignin

source with structural and electrochemical properties of lignin-derived carbon materials. *RSC Adv.* **2018**, *8*, 38721−38732.
(8) Zhao, Y.; Wen, M.; He, C.; Liu, C.; Li, Z.; Liu, Y. Preparation of graphene by catalytic pyrolysis of lignin and its electrochemical properties. *Mater. Lett.* **2020**, *274*, No. 128047.
(9) Wang, X.; Zhu, Y.; Wang, X.; Liu, G.; Li, J.; Zhao, R.; Zhang, Y.; Zhang, X.; Han, G.; Zhao, H.; Yu, J. In-situ growth of graphene on carbon nanofiber from lignin. *Carbon* **2020**, *169*, 446−454.
(10) Yan, Q.; Li, J.; Zhang, X.; Hassan, E. B.; Wang, C.; Zhang, J.; Cai, Z. Catalytic graphitization of Kraft lignin to graphene-based structures with four different transitional metals. *J. Nanopart. Res.* **2018**, *20*, No. 223.
(11) Jeong, K.; Jeong, H. J.; Lee, G.; Kim, S. H.; Kim, K. H.; Yoo, C. G. Catalytic effect of alkali and alkaline earth metals in lignin pyrolysis: a density functional theory study. *Energy Fuels* **2020**, *34*, 9734−9740.
(12) Guo, D. L.; Wu, S. B.; Liu, B.; Yin, X. L.; Yang, Q. Catalytic effects of NaOH and Na_2CO_3 additives on alkali lignin pyrolysis and gasification. *Appl. Energy* **2012**, *95*, 22−30.
(13) Ma, H.; Li, T.; Wu, S.; Zhang, X. Effect of the interaction of phenolic hydroxyl with the benzene rings on lignin pyrolysis. *Bioresour. Technol.* **2020**, *309*, No. 123351.
(14) Lou, R.; Wu, S. B. Products properties from fast pyrolysis of enzymatic/mild acidolysis lignin. *Appl. Energy* **2011**, *88*, 316−322.
(15) Acik, M.; Lee, G.; Mattevi, C.; Chhowalla, M.; Cho, K.; Chabal, Y. J. Unusual infrared-absorption mechanism in thermally reduced graphene oxide. *Nat. Mater.* **2010**, *9*, 840−845.
(16) Li, J.; Pu, G.; Chen, J. S.; Liu, Q. W. High-temperature volatility characteristics and pyrolysis mechanism of common sodium salts. *CIESC J.* **2020**, *71*, 3452−3459.
(17) Si, W.; Zhou, J.; Zhang, S.; Li, S.; Xing, W.; Zhuo, S. Tunable N-doped or dual N, S-doped activated hydrothermal carbons derived from human hair and glucose for supercapacitor applications. *Electrochim. Acta* **2013**, *107*, 397−405.
(18) Wu, F.; Chen, L.; Hu, P.; Wang, Y.; Deng, J.; Mi, B. Industrial alkali lignin-derived biochar as highly efficient and low-cost adsorption material for Pb(II) from aquatic environment. *Bioresour. Technol.* **2021**, *322*, No. 124539.
(19) Yan, Q.; Li, J.; Zhang, X.; Zhang, J.; Cai, Z. In situ formation of graphene encapsulated iron nanoparticles in carbon frames through catalytic graphitization of kraft lignin. *Nanomater. Nanotechnol.* **2018**, *8*, No. 184798041881895.
(20) Liu, F.; Chen, Y.; Gao, J. Preparation and characterization of biobased graphene from Kraft lignin. *BioResources* **2017**, *12*, 6545−6557.
(21) Zhu, J.; Yan, C.; Zhang, X.; Yang, C.; Jiang, M.; Zhang, X. A sustainable platform of lignin: From bioresources to materials and their applications in rechargeable batteries and supercapacitors. *Prog. Energy Combust. Sci.* **2020**, *76*, No. 100788.
(22) Wang, M.; Liu, X.; Song, P.; Wang, X.; Xu, F.; Zhang, X. Transformation of lignosulfonate into graphene-like 2D nanosheets: self-assembly mechanism and their potential in biomedical and electrical applications. *Int. J. Biol. Macromol.* **2019**, *128*, 621−628.
(23) Jordan, R. S.; Wang, Y.; McCurdy, R. D.; Yeung, M. T.; Marsh, K. L.; Khan, S. I.; Kaner, R. B.; Rubin, Y. Synthesis of graphene nanoribbons via the topochemical polymerization and subsequent aromatization of a diacetylene precursor. *Chem* **2016**, *1*, 78−90.
(24) Wu, K.; Yang, C.; Liu, Y.; Liu, C.; Liu, Y.; Lu, H.; Liang, B. Hierarchical meso- and macroporous carbon from lignin for kraft lignin decomposition to aromatic monomers. *Catal. Today* **2021**, *365*, 214−222.
(25) Zhang, L.; You, T.; Zhou, T.; Zhou, X.; Xu, F. Interconnected hierarchical porous carbon from lignin-derived byproducts of bioethanol production for ultra-high performance supercapacitors. *ACS Appl. Mater. Interfaces* **2016**, *8*, 13918−13925.
(26) Tian, W.; Gao, Q.; Tan, Y.; Yang, K.; Zhu, L.; Yang, C.; Zhang, H. Bio-inspired beehive-like hierarchical nanoporous carbon derived from bamboo-based industrial by-product as a high performance supercapacitor electrode material. *J. Mater. Chem. A* **2015**, *3*, 5656−5664.
(27) Li, Z.; Zhang, L.; Amirkhiz, B. S.; Tan, X.; Xu, Z.; Wang, H.; Olsen, B. C.; Holt, C. M. B.; Mitlin, D. Carbonized chicken eggshell membranes with 3D architectures as high-performance electrode materials for supercapacitors. *Adv. Energy Mater.* **2012**, *2*, 431−437.
(28) Jiang, F.; Yao, Y.; Natarajan, B.; Yang, C.; Gao, T.; Xie, H.; Wang, Y.; Xu, L.; Chen, Y.; Gilman, J.; Cui, L.; Hu, L. Ultrahigh-temperature conversion of biomass to highly conductive graphitic carbon. *Carbon* **2019**, *144*, 241−248.
(29) Malard, L.; Pimenta, M. A.; Dresselhaus, G.; Dresselhaus, M. S. Raman spectroscopy in graphene. *Phys. Rep.* **2009**, *473*, 51−87.
(30) Late, D. J.; Maitra, U.; Panchakarla, L. S.; Waghmare, U. V.; Rao, C. N. R. Temperature effects on the Raman spectra of graphenes: dependence on the number of layers and doping. *J. Phys.: Condens. Matter* **2011**, *23*, No. 055303.
(31) Jiang, X. Y.; Lu, Q.; Hu, B.; Chen, D. Y.; Liu, J.; Dong, C. Q. Influence of inherent alkali metal chlorides on pyrolysis mechanism of a lignin model dimer based on DFT study. *J. Therm. Anal. Calorim.* **2019**, *137*, 151−160.
(32) Shi, Y.; Liu, X.; Wang, M.; Huang, J.; Jiang, X.; Pang, J.; Xu, F.; Zhang, X. Synthesis of N-doped carbon quantum dots frombio-waste lignin for selective irons detection and cellular imaging. *Int. J. Biol. Macromol.* **2019**, *128*, 537−545.
(33) Hou, J.; Cao, C.; Idrees, F.; Ma, X. Hierarchical porous nitrogen-doped carbon nanosheets derived from silk for ultrahigh capacity battery anodes and supercapacitors. *ACS Nano* **2015**, *9*, 2556−2564.
(34) Deng, J.; Li, M.; Wang, Y. Biomass-derived carbon: synthesis and applications in energy storage and conversion. *Green Chem.* **2016**, *18*, 4824−4854.
(35) Zhang, X.; Ren, B.; Wu, X.; Yan, X.; Sun, Y.; Gao, H.; Qu, F. Efficient removal of chromium(VI) using a novel waste biomass chestnut shell-based carbon electrode by electrosorption. *ACS Omega* **2021**, *6*, 25389−25396.
(36) Liu, C.; Wang, J.; Li, J.; Zeng, M.; Luo, R.; Shen, J.; Sun, X.; Han, W.; Wang, L. Synthesis of N-doped hollow-structured mesoporous carbon nanospheres for high-performance supercapacitors. *ACS Appl. Mater. Interfaces* **2016**, *8*, 7194−7204.
(37) Li, Y.; Wang, G.; Wei, T.; Fan, Z.; Yan, P. Nitrogen and sulfur co-doped porous carbon nanosheets derived from willow catkin for supercapacitors. *Nano Energy* **2016**, *19*, 165−175.
(38) Biswal, M.; Banerjee, A.; Deo, M.; Ogale, S. From dead leaves to high energy density supercapacitors. *Energy Environ. Sci.* **2013**, *6*, 1249−1259.
(39) Lai, C.; Zhou, Z.; Zhang, L.; Wang, X.; Zhou, Q.; Zhao, Y.; Wang, Y.; Wu, X. F.; Zhu, Z.; Fong, H. Free-standing and mechanically flexible mats consisting of electrospun carbon nanofibers made from a natural product of alkali lignin as binder-free electrodes for high-performance supercapacitors. *J. Power Sources* **2014**, *247*, 134−141.
(40) Jeon, J. W.; Zhang, L.; Lutkenhaus, J. L.; Laskar, D. D.; Lemmon, J. P.; Choi, D.; Nandasiri, M. I.; Hashmi, A.; Xu, J.; Motkuri, R. K.; Fernandez, C. A.; Liu, J.; Tucker, M. P.; McGrail, P. B.; Yang, B.; Nune, S. K. Controlling porosity in lignin-derived nanoporous carbon for supercapacitor applications. *ChemSusChem* **2015**, *8*, 409.
(41) Tian, J.; Lin, C.; Lin, C.; Ma, M. Constructed nitrogen and sulfur codoped multilevel porous carbon from lignin for high-performance supercapacitors. *J. Alloys Compd.* **2019**, *789*, 435−442.
(42) Kawamoto, H. Lignin pyrolysis reactions. *J. Wood Sci.* **2017**, *63*, 117−132.
(43) Chaleawlert-umpon, S.; Pimpha, N. Sustainable lignin-derived hierarchically porous carbon for capacitive deionization applications. *New J. Chem.* **2020**, *44*, 12058−12067.
(44) Cheng, Y.; Zhang, Y.; Meng, C. Template fabrication of amorphous Co_2SiO_4 nanobelts/graphene oxide composites with enhanced electrochemical performances for hybrid supercapacitors. *ACS Appl. Energy Mater.* **2019**, *2*, 3830−3839.

(45) Yu, B.; Chang, Z.; Wang, C. The key pre-pyrolysis in lignin-based activated carbon preparation for high performance supercapacitors. *Mater. Chem. Phys.* **2016**, *181*, 187−193.

https://doi.org/10.1021/acsomega.1c05730
ACS Omega 2021, 6, 34129−34136